life

MDPI

Article

Site-Specific Tumor Dynamics in Zebrafish: Perivitelline Clearance Versus Yolk Sac Dispersion in Breast Cancer Xenografts

Alexandru-Florin Braniște [1,2], Andrei-Nicolae Ceobanu [1,2,3,*], Paula-Alexandra Postu [2] and Gabriel-Mihail Dimofte [4,5]

[1] Doctoral School, Grigore T. Popa University of Medicine and Pharmacy, 700115 Iasi, Romania; braniste.florin@gmail.com
[2] Center for Fundamental Research and Experimental Development in Translation Medicine-TRANSCEND, Regional Institute of Oncology, 700483 Iasi, Romania
[3] Department of Medical Oncology, Regional Institute of Oncology, 700483 Iasi, Romania
[4] 2nd Department of Surgical Oncology, Regional Institute of Oncology, 700483 Iasi, Romania
[5] Department of Surgery, Grigore T. Popa University of Medicine and Pharmacy, 700115 Iasi, Romania
* Correspondence: andreiceobanu@yahoo.com

Abstract

Background: Zebrafish xenografts are increasingly used to study breast cancer, but comparative data on graft persistence and organization across cell lines and implantation sites remain limited, particularly for HER2-positive models. We aimed to characterize the engraftment patterns of four breast cancer cell lines at two implantation sites over four days. Methods: MDA-MB-231, HCC-1806, SK-BR-3 and HCC-1954 cells labelled with CM-DiI were injected into the perivitelline space and yolk sac of Tübingen and Casper zebrafish larvae (*Danio rerio*). Grafts were monitored daily by fluorescence stereomicroscopy to assess area, shape, persistence and dissemination. Results: MDA-MB-231 formed the largest initial grafts, whereas HCC-1954 showed the lowest dissemination frequencies, diverging from SK-BR-3 despite both being HER2-positive. By day 4, primary perivitelline graft signal was absent in SK-BR-3 and HCC-1806 and retained in 17% of MDA-MB-231 and 23% of HCC-1954 xenografts. Yolk sac fluorescence persisted in all lines, although most grafts became disorganized. Dissemination was detected only after perivitelline implantation. Conclusions: These profiles help guide the selection of cell lines, implantation sites and observation windows, while showing that persistent fluorescence does not necessarily represent a stable primary graft.

Keywords: zebrafish; triple-negative breast cancer; HER2-positive breast cancer; perivitelline space; yolk sac; graft clearance; spatial redistribution

Check for updates

Academic Editor: Hung-Chi Cheng

Received: 11 September 2026
Revised: 16 November 2026
Accepted: 19 November 2026
Published: 23 November 2026

Copyright: © 2026 by the authors. Licensee MDPI, Basel, Switzerland. This article is an open access article distributed under the terms and conditions of the Creative Commons Attribution (CC BY) license.

1. Introduction

Breast cancer remains one of the leading causes of cancer-related mortality worldwide and is characterized by considerable biological [1] and clinical heterogeneity [2]. Unlike the hormone-receptor-positive breast cancers which have a better overall prognosis, triple-negative breast cancer (TNBC) [3] and HER2-positive disease [4] are more aggressive and have a higher chance of relapse after curative treatment. This highlights the need for in vivo models capable of assessing individual risk and prognosis, as well as evaluating therapeutic responses.

Larval zebrafish (*Danio rerio*) are increasingly used as a complementary platform to murine xenograft models, offering rapid assays and high-throughput capacity. Zebrafish

xenografts leverage the model's optical clarity and usually utilize fluorescence-based techniques [5]. Another advantage is that grafting can be performed before adaptive immunity matures, four to six weeks after fertilization [6], which removes the need for genetic or pharmacological immunosuppression. However, this permissive window is not immunologically inert: macrophages and neutrophils are already functionally active during the larval stages commonly used for xenografting [7] and can influence whether implanted tumor cells persist, disseminate, or are cleared [8].

These host–tumor interactions make the course of engraftment an important consideration when choosing a xenograft model and its observation window. In fluorescence-based assays, interpretation depends not only on changes in signal intensity but also on how the graft develops and remains measurable over time. The implantation site is relevant in this context: the perivitelline space and yolk sac differ in their physical constraints and accessibility to host cells, and their suitability depends on the cell line and the process being studied [9]. Characterizing graft behavior at each site therefore helps establish what can be assessed and over which period. However, direct comparisons of these two sites in breast cancer xenografts remain limited [10].

For this study, we selected two triple-negative breast cancer cell lines, MDA-MB-231 and HCC-1806, and two hormone receptor-negative, HER2-positive lines, SK-BR-3 [11] and HCC-1954 [12]. MDA-MB-231 provided a reference, given its extensive use in zebrafish and the available data on its engraftment and dissemination [8,13,14]. HCC-1806 allowed a comparison within the same subtype, although previous zebrafish work has largely focused on drug-response assessment [15]. The inclusion of SK-BR-3 and HCC-1954 extended this comparison to HER2-positive disease, for which zebrafish experience is more limited [16]. HCC-1954 has been used to investigate treatment resistance [17], but we found no studies dedicated to characterizing its graft behavior. For SK-BR-3, limited survival following implantation has been reported as an obstacle to evaluating transgene expression [18], raising questions about the conditions under which a graft can be maintained. These gaps leave an incomplete understanding of graft persistence, morphology and dissemination.

Therefore, this study aimed to characterize the engraftment patterns of these four cell lines following implantation into the perivitelline space (PVS) and yolk sac of zebrafish larvae. We recorded graft size and shape at 1 day post-injection (dpi) and followed subsequent changes through 4 dpi to assess the suitability of each implantation site for monitoring these grafts. We also assessed when fluorescence patterns were consistent with clearance or redistribution rather than a stable primary tumor mass.

2. Materials and Methods

2.1. Cell Cultures

Triple-negative breast cancer cell lines MDA-MB-231 (HTB-26) and HCC-1806 (CRL-2335), and HER2-positive cell lines SK-BR-3 (HTB-30) and HCC-1954 (CRL-2338), were obtained from ATCC (Manassas, VA, USA). MDA-MB-231 cells were grown in DMEM/F-12 (11320-074, Gibco, Grand Island, NY, USA), SK-BR-3 cells were grown in McCoy's 5A (30-2007, ATCC), while HCC-1806 and HCC-1954 cells were grown in RPMI-1640 (30-2001, ATCC). All cell culture media were supplemented with 10% fetal bovine serum (F7524, Sigma-Aldrich, St. Louis, MO, USA) and 1% penicillin–streptomycin (P06-07100, PAN Biotech, Aidenbach, Germany). All cell lines were passaged when they reached 80% confluence and maintained at 37 °C in a 5% CO_2 atmosphere.

2.2. Cell Labeling

For each cell line, cell culture medium was removed and the cell monolayer was washed twice with phosphate-buffered saline (PBS) without calcium and magnesium (860015,

Cytion, Heidelberg, Germany). To facilitate detachment, all cell monolayers were treated with PBS containing 1 mM EDTA (15575020, Invitrogen, Carlsbad, CA, USA) for 5 min at 37 °C, followed by incubation with Trypsin-EDTA solution (T4049, Sigma-Aldrich) for 30 s for MDA-MB-231 cells, 2 min for SK-BR-3 and HCC-1954 cells, and 4 min for HCC-1806 cells. The harvested cells were centrifuged at 300× *g* for 5 min at 20 °C and cell number was assessed by hemocytometer counting. Staining was performed with 4 µL Vybrant CM-DiI (V22888, Invitrogen) per 1×10^6 cells in 1 mL incomplete Ham's F-12K (Kaighn's) medium in the dark for 15 min at 37 °C, followed by incubation on ice for 4 min. The dye solution was removed by centrifugation at 300× *g* for 5 min at 20 °C, and the cells were washed with PBS and resuspended in PBS to a final concentration of 5×10^5 cells/µL. Cell viability was quantified by the trypan blue (15250-061, Gibco) exclusion method using an automated cell counter (Accuris Instruments, Edison, NJ, USA) immediately after labelling and again at the end of each injection session, during which the suspension was held on ice for 2–3 h. Mean viability ranged from 82.7% to 94.0% after labelling and from 78.3% to 89.8% at the end of the session ($n = 3$ per cell line).

2.3. Zebrafish Husbandry and Embryo Preparation

Adult zebrafish were housed in a recirculating aquatic system maintained at 28 °C under a 14:10 h light/dark cycle and fed twice daily with commercial dry feed and live Artemia. The wild-type Tübingen and Casper (mitfa^w2/w2; mpv17^a9/a9) lines were obtained from the European Zebrafish Resource Center (KIT, Eggenstein-Leopoldshafen, Germany). PVS and yolk-sac xenografts were performed in both larval strains, although Casper larvae were predominantly used for yolk-sac experiments because the absence of melanic pigmentation facilitated fluorescence-based measurements. Following natural spawning, embryos were collected and transferred to 90-mm Petri dishes containing E3 medium supplemented with 1 mg/L methylene blue, with approximately 50 embryos per dish. Embryos were incubated at 28 °C with daily medium replacement. Unfertilized or non-viable embryos were removed at 24 h post-fertilization (hpf). Embryos remaining inside the chorion at 48 hpf were enzymatically dechorionated using pronase (Sigma-Aldrich, St. Louis, MO, USA, PRON-RO) at 1 mg/mL and thoroughly washed in fresh E3 medium to remove residual enzyme. Because the timing of spontaneous hatching can vary, developmental stage was determined using the morphological criteria described by Kimmel [19]. Embryos displaying developmental delay, morphological abnormalities or damage resulting from iatrogenic procedures were discarded. Selected 48 hpf embryos were maintained at approximately 50 embryos per dish until injection, at which point they were anesthetized using tricaine (Sigma-Aldrich, E10521) at a final concentration of 150 mg/L.

2.4. Zebrafish Xenografting

CM-DiI-labelled MDA-MB-231, HCC-1806, SK-BR-3 and HCC-1954 cells were prepared for microinjection at a final concentration of 5×10^5 cells/µL in PBS. During injection sessions, the cell suspension was kept on ice and gently resuspended approximately every 20 min to limit sedimentation while avoiding air bubbles. Approximately 5 µL of suspension was back-loaded into pulled borosilicate glass capillaries using 0–200 µL tapered gel-loading tips (Dacchim, Bucharest, Romania, 10.200079). Borosilicate glass capillaries without filament (World Precision Instruments, Sarasota, FL, USA, TW100-4) were pulled with a Narishige PB-7 needle puller (Narishige, Tokyo, Japan). Immediately before use, the tapered tip was empirically trimmed with fine forceps to permit continuous flow of the cell suspension without tip obstruction. Microinjections were performed under a Zeiss Stereo Lumar V12 stereomicroscope using a MINJ-1 pneumatic microinjector connected to a MINJ-2 pulse control module and MINJ-4 holder (Tritech Research, Los Angeles, CA, USA).

For injection, 48 hpf anesthetized embryos were aligned on 2% agarose plates. For PVS microinjection, the capillary was advanced from the dorsal aspect of the embryo and positioned to deposit the cellular bolus within the anterior perivitelline space, while avoiding the cardiac region and visible vascular entry. For yolk-sac microinjection, cells were deposited centrally into the yolk-sac compartment, away from the duct of Cuvier (DoC). Larvae were screened via brightfield and fluorescence stereomicroscopy during and immediately following injection. Any individual failing to meet the criteria was discarded. Because resistance to injection differed between embryos and between anatomical compartments, the injected volume was not defined by oil calibration or by a fixed pulse-derived volume. Instead, pressure pulses were adjusted manually to deposit a visually comparable cellular bolus, approximately similar in size to the embryonic eye, following an established zebrafish xenograft microinjection approach [20]. This procedure was used to minimize variation in initial cell delivery while avoiding volume-induced tissue damage, although small differences in the number of cells deposited cannot be completely excluded. All four breast cancer cell lines were injected into both the PVS and yolk sac. After the procedure, larvae were rinsed through three successive E3 medium baths over approximately 15 min to remove residual anesthetic and were then transferred to fresh E3 medium. Injected larvae were maintained at 34 °C, as a physiological compromise between zebrafish larvae tolerance and human cancer cell thermal requirements [21], with approximately 50 larvae per Petri dish, and the medium was replaced daily.

At 1 dpi, baseline quality screening was performed. Larvae were excluded if they exhibited mortality, severe axial malformations, extensive cardiac or yolk-sac edema, off-target bolus localization or poorly consolidated cell clusters. Mild post-injection cardiac edema was not an automatic exclusion criterion provided the fish remained viable and the xenograft was correctly localized. Larvae meeting inclusion criteria were transferred individually to 24-well plates, with one per well, allowing each xenograft to be monitored separately throughout the experiment.

Assessments were conducted up to 4 dpi, with daily imaging of both PVS and yolk-sac xenografts. High-magnification video recordings were performed in a small exploratory subset of yolk-sac-injected larvae to qualitatively track fluorescent signal redistribution. Additionally, a small group of HCC-1954 embryos was injected through the DoC as a technical reference for vascular delivery. These larvae were imaged at 1 dpi only and were excluded from the main PVS and yolk-sac analyses.

Additional control experiments were performed to evaluate CM-DiI-associated fluorescence independently of the main viable-cell xenograft experiments. For the cell-free control, a solution containing 4 µL CM-DiI in 1 mL incomplete Ham's F-12K medium, without cells, was injected into the PVS or yolk sac of Casper larvae ($n = 7$ per group). Larvae were imaged immediately after injection and monitored daily through 4 dpi.

For the heat-treated-cell control, MDA-MB-231 cells were labeled with CM-DiI and washed according to the procedure described above. Cells were subsequently resuspended in PBS and incubated in a water bath at 60 °C for 20 min with gentle agitation. Cell viability was assessed using the Trypan Blue exclusion method before and after heat treatment. Heat-treated cells were injected into the PVS ($n = 7$) or yolk sac ($n = 15$) using the previously described microinjection procedure and were monitored daily through 4 dpi. Additionally, viable and heat-treated CM-DiI-labeled MDA-MB-231 cells were maintained in parallel cultures under the same temperature and atmospheric conditions used for zebrafish xenograft incubation (34 °C) and imaged daily to compare their morphology, adherence, and fluorescence persistence.

2.5. Clodronate Liposome Co-Injection

To explore whether host phagocytic cells contributed to the loss of the PVS graft, SK-BR-3 cells were co-injected with clodronate liposomes (Liposoma, Amsterdam, The Netherlands). Immediately before injection, the SK-BR-3 cell suspension prepared at approximately 5×10^5 cells/μL was allowed to sediment briefly. Supernatant was removed and replaced with clodronate liposome stock suspension (5 mg/mL clodronate), maintaining the cell concentration used for standard injections. The mixture was resuspended and back-loaded into a pulled capillary. Co-injection was performed following the same anterior PVS microinjection protocol, post-injection handling, 1 dpi screening procedure, and daily imaging schedule described for standard PVS xenografts. The control group consisted of SK-BR-3 cells injected without clodronate liposomes. Larvae were also injected in the PVS with a mixture of CM-DiI-labelled liposomes (Liposoma, The Netherlands) and either clodronate liposomes or PBS, to monitor survival over the same observation window. To confirm the phagocyte-depleting effect of clodronate liposomes, an additional experiment was performed in Casper larvae using Neutral Red vital staining, as described by Yang et al. [22]. Uninjected larvae served as controls, while the remaining groups received PBS, CM-DiI-labelled liposomes, or clodronate liposomes into either the PVS or yolk sac. Neutral Red-positive brain microglia were then counted individually using stereomicroscopy.

2.6. Fluorescence Imaging

Fluorescence imaging was performed using a Zeiss Stereo Lumar V12 fluorescence stereomicroscope equipped with an HBO100 illuminator (Carl Zeiss Microscopy GmbH, Jena, Germany) and a Retiga 6000 camera (QImaging, Surrey, BC, Canada). At each imaging time point, larvae were anesthetized with tricaine and positioned laterally on 2% agarose plates to allow standardized visualization of the xenograft region and whole-larva fluorescent cell distribution.

2.7. Image Analysis and Measured Variables

Images were analyzed in Fiji v1.54t [23]. For each larva, the CM-DiI fluorescence channel was reviewed alongside the corresponding bright-field image to orient the specimen and assign fluorescent signals to the implantation site or anatomical regions of interest. To isolate tumor-derived signal from host autofluorescence and background noise, the threshold was manually adjusted for each image by a single operator blinded to experimental group allocation. Signal was retained as tumor-associated when it was distinctly brighter than the surrounding tissue, located within one of the anatomical regions defined below, and appeared either as a compact aggregate (primary implantation-site mass or tail metastatic focus [TMF]) or as discrete, spatially separated events (circulating cells [CC]). Diffuse low-intensity background, yolk autofluorescence, isolated single pixels and obvious specular reflections were excluded. Fluorescence intensity was not used as a quantitative endpoint. All measurements described below were performed on thresholded CM-DiI signal, referred to hereafter as tumor-associated signal; this terminology is used for readability and does not imply that every fluorescent object was independently verified as an intact tumor cell.

The primary tumor mass was defined as the compact aggregate of tumor-associated signal at the expected implantation site, and its presence or absence was scored daily in both PVS- and yolk-sac-injected larvae. Area was quantified within this mass alone, at the PVS or the yolk sac according to the injection site, and recorded as 0 when no primary signal remained visible. Tumor shape was described by sphericity, defined as the maximum horizontal diameter (A) divided by the maximum vertical diameter (B) of the tumor-associated mass. Values approaching 1 indicate a more spherical morphology, whereas values below or above 1 indicate preferential vertical or horizontal elongation, respectively.

An annotated representative example of the measurements used to calculate sphericity is provided in Figure S1. Both were measured at 1 dpi at each site. At 4 dpi, yolk-sac grafts were additionally scored as structured or unstructured, a structured mass being compact and homogeneous and an unstructured one diffuse or fragmented.

Dissemination was scored in both PVS and yolk-sac-implanted larvae using identical criteria. For PVS xenografts, CC analysis was restricted to 1 dpi: by 4 dpi the primary PVS mass had largely dispersed and fluorescent events were distributed across the body, so signal outside the implantation site could no longer be reliably attributed to dissemination. TMF, being morphologically distinct, were recorded at both 1 and 4 dpi. CC were classified as fluorescent, tumor-associated events visible beyond the injection site, with a minimum threshold of ten events required to score a positive result, thereby minimizing false positives from isolated artifacts. The threshold of at least ten fluorescent events for CC classification was selected based on preliminary pilot observations, in which isolated fluorescent signals were detected without accompanying TMF. This operational criterion was subsequently applied consistently across all experimental groups to avoid classifying occasional fluorescent events as CC. They were further classified by location as tail-associated or non-tail-associated, the latter defined as CC outside the primary implantation site, yolk-sac region, DoC, cardiac region and tail, corresponding mainly to the anterior/head–branchial region. Imaging-defined TMF were recorded separately: compact aggregates in the tail region composed of at least five grouped cell-like events and showing a clustered rather than linear distribution. CC and TMF were analyzed as binary endpoints, recorded as present or absent. These definitions were necessary to specifically address the optical limitations and the resolution constraints of the fluorescence stereomicroscopy.

2.8. Statistical Analysis

Statistical analyses were performed using GraphPad Prism version 10. Comparisons of primary tumor area and sphericity across the four cell lines were performed using the Kruskal–Wallis test, followed by Dunn's multiple comparisons test for pairwise comparisons. Primary tumor persistence and survival following clodronate co-injection were analyzed using the Kaplan–Meier method, with groups compared by the log-rank (Mantel–Cox) test. CC, TMF, and structured/unstructured proportions were binary endpoints and are reported descriptively. Sample sizes for each analysis are reported in the corresponding figure legends. A p-value of less than 0.05 was considered statistically significant.

2.9. Ethics Statement

All experimental procedures were conducted in accordance with institutional animal welfare regulations and applicable national and European legislation implementing Directive 2010/63/EU on the protection of animals used for scientific purposes. The study protocol was approved by the ethics committees of the Alexandru Ioan Cuza University of Iasi, Romania (Approval No. 693/11 February 2026), Grigore T. Popa University of Medicine and Pharmacy, Iasi, Romania (Approval No. 257/17 January 2023), and the Regional Institute of Oncology, Iasi, Romania (Approval No. 1394/29 November 2022). Only established, commercially available human cell lines were utilized; no primary human tissues, patient-derived xenografts, or identifiable clinical data were involved in this work.

3. Results

3.1. Cell Line and Implantation Site Shape Early Xenograft Readouts

At 1 dpi, the four cell lines generated visibly different primary tumors within the PVS compartment (Figure 1A). The clearest difference was in primary tumor area ($p < 0.0001$, overall; Figure 1B): MDA-MB-231 formed the largest implants, exceeding HCC-1806

($p = 0.0451$), HCC-1954 ($p < 0.0001$) and SK-BR-3 ($p < 0.0001$), while the remaining three lines did not differ significantly from one another. Early size variation in this compartment was therefore driven almost entirely by MDA-MB-231.

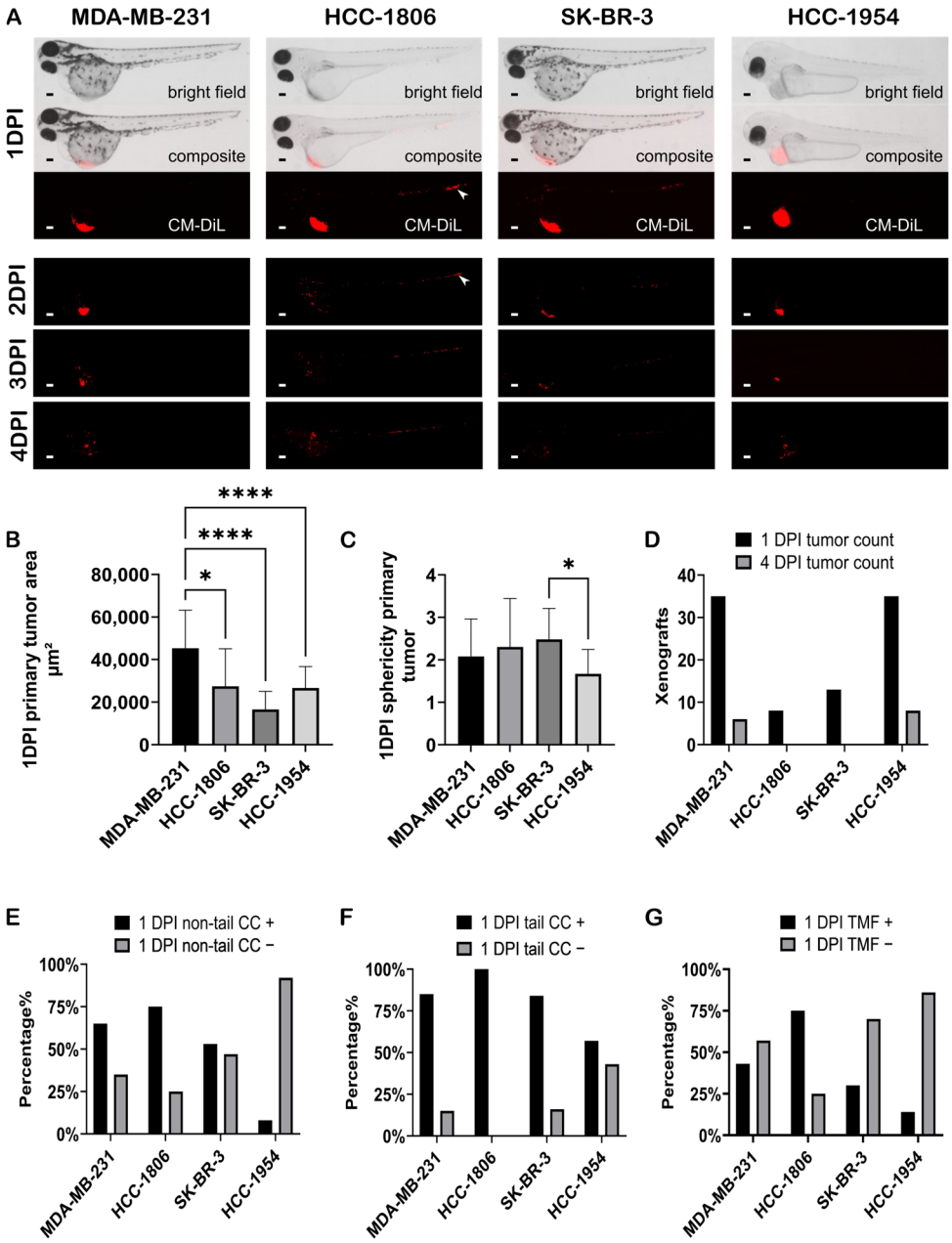

Figure 1. Early characteristics and temporal evolution of PVS xenografts across breast cancer cell lines. (**A**) Representative bright-field, composite and CM-DiI fluorescence stereomicroscopy images of MDA-MB-231, HCC-1806, SK-BR-3 and HCC-1954 xenografts from 1 to 4 dpi, illustrating the progressive reduction and loss of the primary PVS tumor signal by 4 dpi. Arrowheads highlight the disappearance of a representative tail metastatic focus (TMF) over time. (**B**) Primary tumor area and (**C**) sphericity at 1 dpi (measured as maximum horizontal diameter/maximum vertical diameter of the tumor). (**D**) Number of xenografts with a detectable primary tumor at 1 and 4 dpi. Proportions of xenografts positive or negative for (**E**) non-tail circulating cells (CC), (**F**) tail-associated CC and (**G**) TMF at 1 dpi. Sample sizes and strain composition (Tübingen/Casper): $n = 35$, 14/21 (MDA-MB-231); $n = 8$, 4/4 (HCC-1806); $n = 13$, 3/10 (SK-BR-3); $n = 35$, 13/22 (HCC-1954). Statistical comparisons in (**B**,**C**) were performed using the Kruskal–Wallis test followed by Dunn's multiple-comparisons test. * $p < 0.05$; **** $p < 0.0001$. Scale bar, 100 µm.

Projected shape was more consistent across the cell lines. The A/B ratio differed between lines overall ($p = 0.0083$), but only SK-BR-3 and HCC-1954 were significantly different ($p = 0.0119$; Figure 1C). A key observation is that HCC-1954 showed the most spherical projected morphology, whereas the other lines exhibited a more elongated morphology. PVS xenografts also generated fluorescent signal outside the implantation site by 1 dpi, allowing dissemination to be scored at the same time point. Non-tail CC were frequently observed in MDA-MB-231, HCC-1806 and SK-BR-3 xenografts (54–75%), while being largely absent in HCC-1954 (9%; Figure 1E). Tail CC were present in all four models, with HCC-1954 showing the lowest frequency (57% compared to 85–100% in other lines; Figure 1F). TMF was also identified in every cell line at 1 dpi, ranging from 75% in HCC-1806 to 14% in HCC-1954 (Figure 1G). All three readouts ranked the cell lines in the same order, and compact foci were consistently less frequent than dispersed events. Across all three, HCC-1954 ranked lowest despite forming grafts comparable in area to HCC-1806 and SK-BR-3. Early dissemination therefore did not simply correlate with primary tumor size.

The yolk sac reproduced the size differences seen in the PVS but not the dissemination. At 1 dpi the signal within the yolk sac remained well organized (Figure 2A), and its area also differed between lines ($p = 0.0007$ overall; Figure 2B): MDA-MB-231 generated the largest yolk-sac tumor-associated area, significantly exceeding SK-BR-3 ($p = 0.0018$) and HCC-1954 ($p = 0.0037$) but not HCC-1806 ($p = 0.1066$); no other comparison reached significance.

Because the signal remained organized at this time point, the projected shape could also be described at this site. The A/B ratio differed between lines ($p = 0.0016$ overall; Figure 2C). As in the PVS, HCC-1954 showed the sphericity value closest to 1, differing significantly from MDA-MB-231 ($p = 0.0007$) and HCC-1806 ($p = 0.0354$). However, the values are not directly comparable between compartments, since the yolk-sac measurement describes the spread of the deposit within a large ovoid space rather than the shape of a free-standing mass. Unlike PVS injection, yolk-sac injection was not associated with detectable CC or TMF. Cell-line differences in tumor-associated area were therefore preserved at both sites, but dissemination was detectable only after PVS implantation.

3.2. PVS and Yolk-Sac Xenografts Diverge over the 4-Day Observation Window

Over the 4-day window the two implantation sites diverged sharply (Figures 1 and 2).

In the PVS, the primary tumor signal decreased substantially between 1 and 4 dpi. Although every larva included at 1 dpi screening presented with a distinct primary PVS graft, only a minority retained a recognizable primary tumor at the injection site by 4 dpi. Residual primary tumors were observed in MDA-MB-231 (17%) and HCC-1954 (23%), whereas SK-BR-3 and HCC-1806 showed complete loss of visible primary PVS signal by the end of the observation window (Figure 1D). Representative daily images illustrate the progressive reduction in primary tumor signal across the four cell lines (Figure 1A). TMF followed the same pattern. Frequency decreased in every cell line between 1 and 4 dpi, and no line generated foci that had not already been present at 1 dpi. By 4 dpi TMF persisted only in MDA-MB-231 (11.4%) and HCC-1954 (6%), the same two lines that retained primary signal, and were absent from HCC-1806 and SK-BR-3, which had lost it. The progressive disappearance of a representative TMF is illustrated in Figure 1A.

The yolk sac behaved differently: all yolk-sac xenografts remained detectable at 4 dpi. Persistence of fluorescence did not, however, imply maintenance of a compact and spatially stable primary tumor. Over time, the fluorescent signal became increasingly redistributed within the yolk sac, resulting in a more diffuse appearance by the end of the assay (Figure 2A). Only a minority of yolk-sac grafts were classified as structured at 4 dpi, and the proportion was similar across cell lines (30–40%; Figure 2D). High-magnification recordings of a small exploratory subset showed fluorescent cell clusters within the yolk-sac compart-

ment shifting position during larval movement and adjacent organ movement (Video S1). These observations were not quantified, but they are consistent with a mechanical contribution to the dispersion of cells within the yolk sac, rather than cell-specific properties. No CC or TMF were detected in any yolk-sac group at any of the four daily assessments. The two sites therefore showed different dynamics over the same interval: the PVS lost primary tumor signal, whereas the yolk sac retained signal that became progressively less organized.

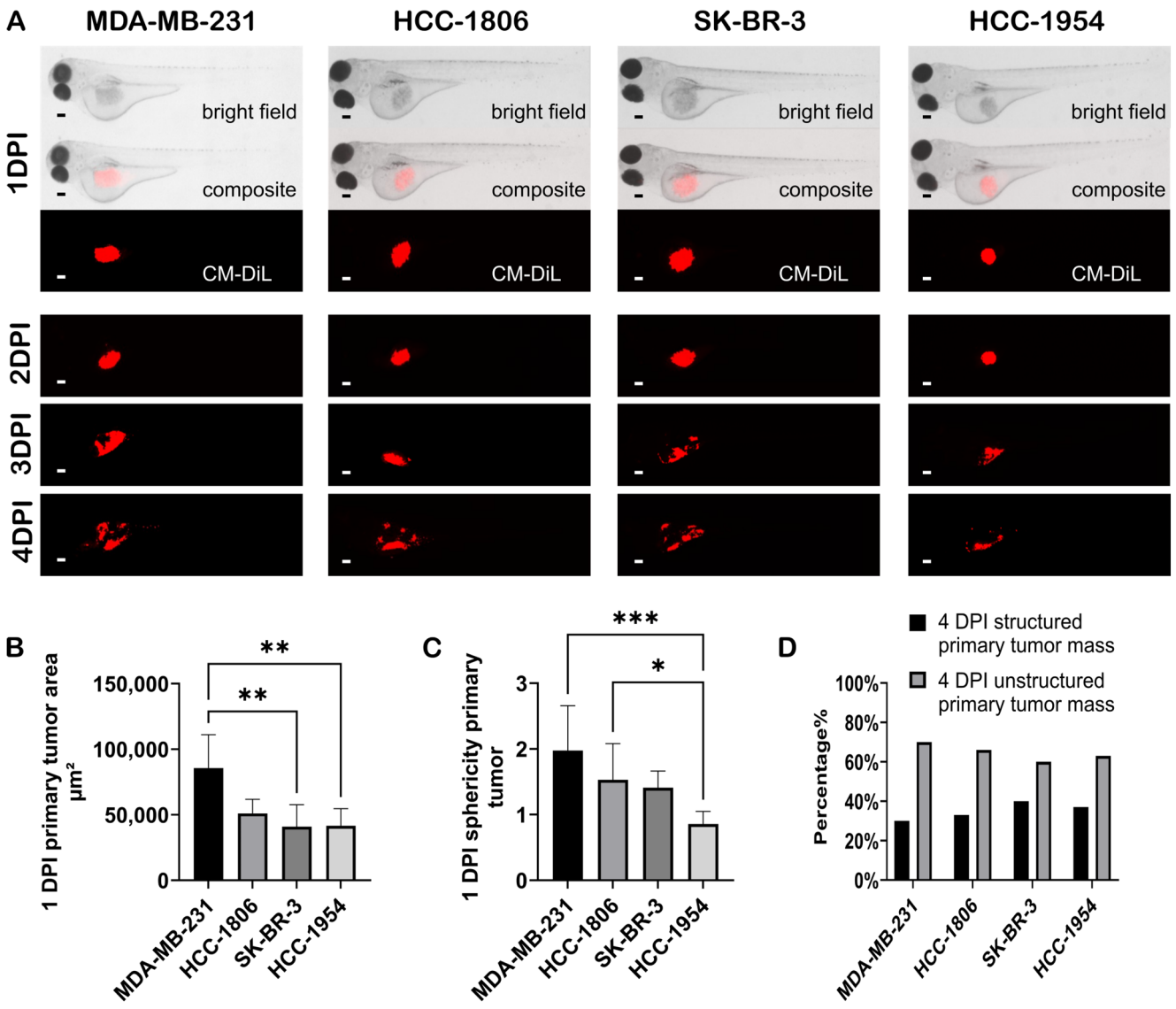

Figure 2. Early characteristics and temporal evolution of yolk-sac xenografts across breast cancer cell lines. (**A**) Representative bright-field, composite and CM-DiI fluorescence stereomicroscopy images of MDA-MB-231, HCC-1806, SK-BR-3 and HCC-1954 xenografts from 1 to 4 dpi, illustrating persistence of tumor-associated fluorescence together with progressive redistribution and loss of organization within the yolk sac. (**B**) Primary tumor-associated area and (**C**) sphericity at 1 dpi (measured as maximum horizontal diameter/maximum vertical diameter of the tumor). (**D**) Proportions of xenografts classified as structured or unstructured at 4 dpi, showing a predominance of unstructured signals across all four cell lines. No circulating cells (CC) or tail metastatic foci (TMF) were detected in yolk-sac xenografts at any time point during the four-day observation period. Sample sizes and strain composition (Tübingen/Casper): $n = 10$, 3/7 (MDA-MB-231); $n = 9$, 2/7 (HCC-1806); $n = 10$, 3/7 (SK-BR-3); $n = 8$, 2/6 (HCC-1954). Statistical comparisons in (**B**,**C**) were performed using the Kruskal–Wallis test followed by Dunn's multiple-comparisons test. * $p < 0.05$; ** $p < 0.01$; *** $p < 0.001$. Scale bar, 100 µm.

3.3. Clodronate Prolongs SK-BR-3 PVS Signal Persistence

To investigate whether graft retention could be prolonged through 4 dpi, we selected SK-BR-3 because it formed the smallest primary tumors at 1 dpi (Figure 1B). Co-injection with clodronate liposomes substantially increased the graft persistence at 4 dpi with approximately 90% of clodronate-treated SK-BR-3 xenografts retaining a visible primary tumor mass, so the median persistence was not reached within the observation window ($p < 0.0001$; Figure 3B). Representative daily images are shown in Figure 3A.

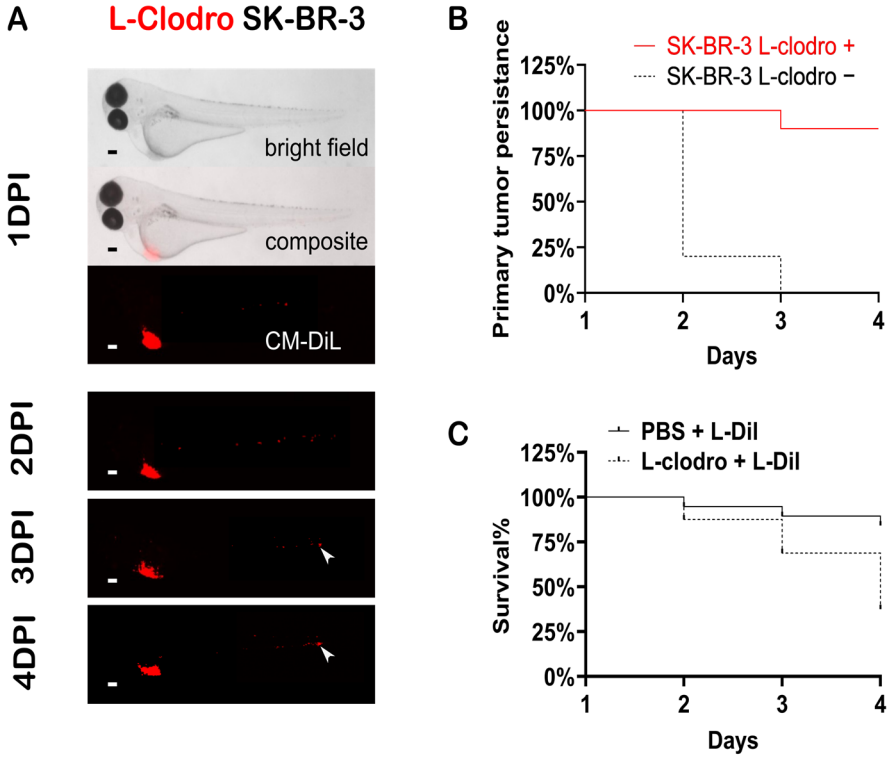

Figure 3. Clodronate liposome co-injection prolongs SK-BR-3 PVS xenograft persistence. (**A**) Representative bright-field, composite and CM-DiI fluorescence stereomicroscopy images of SK-BR-3 xenografts co-injected with clodronate liposomes from 1 to 4 dpi, showing prolonged retention of the primary PVS tumor signal. Arrowheads indicate the appearance of a tail metastatic focus (TMF) after 1 dpi. (**B**) Primary tumor persistence in SK-BR-3 xenografts with or without clodronate liposome co-injection (clodronate-treated: $n = 10$, 7/3 Tübingen/Casper; untreated: $n = 13$, 3/10 Tübingen/Casper). (**C**) Survival of larvae injected with CM-DiI-labelled liposomes combined with clodronate liposomes or PBS (clodronate: $n = 16$, 1/15 Tübingen/Casper; PBS: $n = 19$, 2/17 Tübingen/Casper). Statistical comparisons in (**B**,**C**) were performed using the log-rank (Mantel–Cox) test; $p < 0.0001$ for primary tumor persistence and $p = 0.0065$ for survival. Scale bar, 100 µm.

TMF followed different patterns in the two groups. At 1 dpi TMF were present in 31% of untreated larvae and in none of the clodronate-treated larvae; by 4 dpi the numbers were reversed, with TMF in 30% of clodronate-treated larvae and none of the untreated controls (Figure 3A). In untreated xenografts, early TMF cleared over time and no new foci formed, whereas in clodronate-treated larvae, new foci emerged by 4 dpi that were not observed at 1 dpi. Given the small exploratory sample and the absence of a prespecified statistical comparison, these observations are reported descriptively.

To test whether clodronate liposomes also affected host viability independently of tumor behavior, a separate control experiment used CM-DiI-labelled liposomes in the absence of tumor cells. Larvae injected with a mixture of CM-DiI-labelled liposomes and clodronate liposomes showed reduced survival compared with larvae injected with CM-

DiI-labelled liposomes mixed with PBS ($p = 0.0065$; Figure 3C). Clodronate co-injection thus prolonged SK-BR-3 primary tumor persistence, but at a measurable survival cost.

To validate the effect of clodronate liposomes, brain microglia were quantified by Neutral Red staining at 2 dpi. Microglial counts differed significantly across the experimental groups ($p = 0.0003$). Clodronate administration into the PVS markedly reduced the number of Neutral Red-positive microglia by more than 80% compared with PBS-PVS controls ($p = 0.003$). In contrast, no statistically significant differences in microglial counts were observed among the remaining six experimental groups (all adjusted $p > 0.9999$) (Figure S8).

3.4. Fluorescence Distribution and Control Experiments

As a technical reference for distinguishing localized cell deposition from vascular distribution, we compared representative fluorescence patterns at 1 dpi after PVS, yolk-sac and DoC injection (Figure 4). Yolk-sac injection generated a well-defined signal confined to the yolk compartment, whereas PVS injection produced a compact anterior perivitelline mass. DoC injection produced the expected intravascular distribution, with fluorescent cells visible in circulation, accumulating in the caudal region and in anterior/head–branchial vascular territories. This group therefore served as a visual anatomical reference for the anatomical classification used in dissemination scoring, supporting the distinction between tail-associated and non-tail-associated CC in PVS and yolk-sac-injected larvae. Both caudal morphologies were visible after DoC delivery: dispersed cell-like events and compact clustered foci, resembling the patterns scored as CC and TMF, respectively (Figure 4).

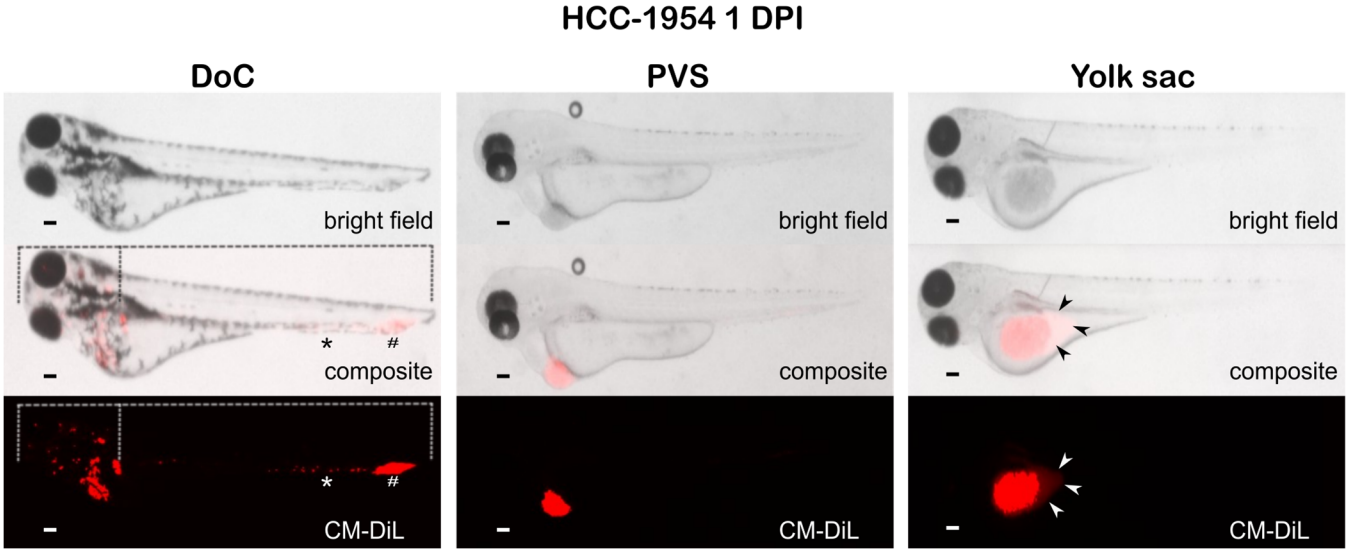

Figure 4. Representative distribution of HCC-1954 cells according to injection site at 1 dpi. Bright-field, composite and CM-DiI fluorescence stereomicroscopy images following injection into the duct of Cuvier (DoC), perivitelline space (PVS) or yolk sac. DoC injection produced an intravascular distribution involving anterior/head–branchial and caudal territories. Dashed lines separate the non-tail and tail regions used for dissemination scoring; tail-associated CC (*) and TMF (#) are indicated. PVS and yolk-sac injections produced localized signals at the respective implantation sites. Arrowheads indicate apparent fluorescence enlargement due to reflection, emphasizing the need for concurrent bright-field assessment. Representative strains: DoC, Tübingen; PVS and yolk sac, Casper. Scale bar, 100 µm.

To further characterize the observed fluorescence patterns, two additional control experiments were performed. Cell-free CM-DiI injection produced no detectable dye-

associated fluorescent signals immediately after injection or during the subsequent four-day observation period, irrespective of the implantation site (Figure S2).

Following heat treatment, MDA-MB-231 cells showed increased Trypan Blue uptake, consistent with markedly reduced viability, while CM-DiI-associated fluorescence remained detectable. In yolk-sac xenografts, heat-treated cells produced significantly smaller fluorescent areas than viable cells at 1 dpi ($p = 0.0002$), although fluorescence persisted and underwent redistribution through 4 dpi.

Following PVS implantation, fluorescent areas were also significantly smaller in the heat-treated group ($p < 0.0001$). Tail-associated CC were detected in 30/35 viable-cell xenografts compared with 2/7 heat-treated controls ($p = 0.0049$), while TMF were observed in 15/35 viable-cell xenografts and none of the heat-treated controls ($p = 0.0382$). At 4 dpi, primary PVS fluorescence remained detectable in 6/35 viable-cell xenografts compared with 0/7 heat-treated controls. Detailed results and representative images are provided in the Supplementary Materials (Figures S3–S7).

4. Discussion

Zebrafish xenograft studies commonly use fluorescence imaging to monitor graft size, follow the distribution of cells and assess treatment responses over short observation periods. Here, we compared four breast cancer cell lines in the PVS and yolk sac to assess graft persistence and organization from 1 to 4 dpi. The comparison revealed two different limitations: frequent loss of primary graft signal in the PVS and progressive disorganization despite persistent fluorescence in the yolk sac. Longer signal retention therefore did not necessarily mean that a distinct primary graft remained available for measurement. These findings highlight the importance of considering both graft persistence and organization when choosing an implantation site and observation period.

The marked loss of primary PVS signal raises the question of which factors govern graft maintenance within this compartment. At this developmental stage, zebrafish phagocytes patrol both the circulation and extravascular tissues, allowing early immune access without direct vascular contact [7]. In colorectal zebrafish xenografts, macrophages and neutrophils have been shown to actively clear poorly engrafting SW480 cells, indicating that graft loss can reflect immune-mediated elimination rather than simply limited proliferation [8]. Poor SK-BR-3 survival has also been reported in a nanoparticle-delivery study, where it prevented assessment of transgene expression [18]. In our study, clodronate liposome co-injection prolonged SK-BR-3 graft persistence, with approximately 90% of treated xenografts retaining a visible primary mass at 4 dpi, compared with none of the untreated controls. This suggests that host phagocytic activity may contribute to primary graft loss. Macrophage depletion following clodronate liposome administration has previously been demonstrated in zebrafish larvae [22]. Consistent with these findings, our Neutral Red experiment confirmed a marked reduction in brain microglia following PVS administration of clodronate liposomes, supporting the involvement of host phagocytic cells in the observed graft clearance.

In untreated xenografts, TMF persisted at 4 dpi only in MDA-MB-231 and HCC-1954, the same two lines that retained primary PVS signal. Both signals were absent in HCC-1806 and SK-BR-3. In clodronate-treated SK-BR-3 larvae, TMF appeared after 1 dpi, whereas foci in untreated SK-BR-3 controls were already present at the first assessment and subsequently disappeared. These observations suggest that phagocytic clearance may contribute to the loss of both primary graft signal and tail foci.

Clodronate liposomes also reduced larval survival in the separate experiment without tumor cells. The potential use of clodronate to extend graft monitoring must therefore be considered alongside host tolerability.

In contrast to the loss of primary PVS signal, fluorescence remained detectable in all four cell lines in the yolk sac at 4 dpi. However, only approximately 30–40% of xenografts retained their initially structured appearance. The yolk is comparatively poorly vascularized and has been reported to show lower macrophage infiltration than the PVS in other zebrafish xenograft studies [24], which may limit the clearance mechanism proposed for the PVS and help explain why fluorescence persisted despite the loss of structure. The similar loss of organization across cell lines suggests a shared influence of the yolk environment. Developmental remodeling is likely to contribute, as yolk reserves are largely depleted by 5–6 days post-fertilization (3–4 dpi) under standard rearing conditions [25], while elevated incubation temperatures have been shown to accelerate yolk utilization in developing zebrafish [26]. The yolk also represents a viscous, largely acellular environment that provides limited anchorage [10]. This contrasts with the more spatially constrained environment of the PVS and may contribute to the different organization of grafts at the two sites. Our recordings showed that fluorescent material shifted with larval movement and organ activity, making passive mechanical redistribution a plausible contributing factor.

No CC or TMF were detected after yolk-sac implantation, in contrast to previous reports of dissemination from this compartment. Several methodological differences may help explain this discrepancy. Our definition of CC positivity required at least ten events, whereas other studies have used thresholds above five cells, based on the observation that non-metastatic lines did not exceed this level [27]. MDA-MB-231 cells have also been reported to disseminate relatively slowly from the yolk sac, with only a few larvae showing tail intravasation even after five days, whereas selected, more invasive subpopulations reached higher frequencies within one to three days [28]. In addition, studies demonstrating clear dissemination from the yolk have relied on confocal microscopy [29], which offers greater sensitivity for detecting small numbers of dispersed cells. The absence of CC and TMF in our yolk cohorts should therefore be interpreted within the sensitivity, scoring criteria, and observation window of the present study rather than as evidence that these lines are intrinsically unable to leave this compartment.

After PVS implantation, dissemination frequencies varied among cell lines and did not follow the same pattern as initial graft area. Across all four lines, tail CC frequencies exceeded non-tail CC frequencies, consistent with preferential accumulation of fluorescent events within the caudal region, potentially reflecting vascular arrest of tumor cells [30]. HCC-1954 nevertheless ranked lowest across all dissemination readouts despite forming PVS implants comparable in area to HCC-1806 and SK-BR-3, which showed the highest tail CC and TMF frequencies. Immunohistochemical profile alone also failed to explain this pattern, as SK-BR-3 showed dissemination frequencies closer to those of the TNBC lines than to HCC-1954.

One possible explanation is variation in cell–cell cohesion. HCC-1954 has been described as forming compact spheroids and retaining strong E-cadherin expression, whereas SK-BR-3 forms looser aggregates and lacks functional E-cadherin. Consistent with this, HCC-1954 showed the sphericity value closest to 1 among the four cell lines at 1 dpi and differed significantly from SK-BR-3. MDA-MB-231 and HCC-1806 form irregular clumps with a more compact center in the same morphological study, not cleanly matching either category [31–35]. Interactions with the surrounding stroma may also influence graft behavior. HCC-1954 becomes invasive when cocultured with human stromal fibroblasts [36], a component of breast tumors [37], absent in the zebrafish model.

The principal methodological limitation concerns the fluorescent label itself. CM-DiI is widely used in zebrafish xenograft studies because its red emission is compatible with GFP-based reporter lines, while reports of leakage with alternative dyes, such as CellTracker Green CMFDA, have also favored its use [20]. Nevertheless, CM-DiI can persist in dead

cells and cellular debris, transfer to unlabeled cells, and be taken up by host phagocytes [9]. A direct comparison of DiI and GFP labeling in zebrafish-xenografted MDA-MB-231 cells similarly demonstrated that DiI-based measurements may overestimate tumor growth [38]. To minimize potential interpretation bias, fluorescence images were consistently evaluated alongside corresponding bright-field images, and the same anatomical, numerical, and morphological criteria were applied across experimental groups. In particular, the threshold of at least ten fluorescent events for CC classification was informed by preliminary pilot observations and was intended to avoid classifying isolated fluorescent signals as CC. These criteria supported standardized comparisons but were not intended to independently establish the cellular identity or viability of every fluorescent event.

The additional control experiments further clarified the interpretation of CM-DiI-associated fluorescence in our model. Cell-free CM-DiI injections produced no detectable dye-associated fluorescent signal, whereas fluorescence remained detectable following injection of heat-treated, CM-DiI-labeled MDA-MB-231 cells. Interestingly, the behavior of this fluorescent material differed between implantation sites. In the yolk sac, fluorescence persisted and underwent redistribution following heat-treated-cell injection, resembling patterns observed with viable cells. This supports our hypothesis that mechanical redistribution contributes to the changes in fluorescence organization within this compartment, which may therefore not exclusively reflect intrinsic tumor-cell properties during the four-day observation period. In contrast, following PVS implantation, CC were significantly less frequent in the heat-treated group, while TMF were observed exclusively following viable-cell injection. These findings support a contribution of viable tumor-cell behavior to the formation of organized tail-associated foci. Overall, the additional controls refine the interpretation of our fluorescence-based observations while preserving the comparative value of the study, which was designed to characterize the early behavior of four breast cancer cell lines at two implantation sites. Future investigations requiring further confirmation of cellular identity or viability could employ genetically encoded fluorescent reporters, confocal imaging, human-specific immunofluorescent markers such as anti-human mitochondria, or flow cytometry with appropriate cell-identity and viability markers. Similarly, direct visualization of host immune-cell interactions with the xenografts was not possible without transgenic immune reporters.

Both Tübingen and Casper larvae were included in the study, with their distribution across experimental groups reported in the figure legends. Although primary PVS grafts were readily distinguishable due to their superficial and well-defined location, and fluorescent signals in the yolk sac, caudal and non-caudal regions were generally detectable, differences in pigmentation could influence the sensitivity of fluorescence detection, particularly for weak signals. However, a strain-specific comparison of MDA-MB-231 xenografts at 1 dpi revealed no statistically significant differences between Tübingen and Casper larvae in the detection of tail-associated CC ($p = 0.3691$) or non-tail CC ($p = 0.1534$; Figure S9).

Beyond these imaging-related constraints, the larval zebrafish host imposes additional physiological limitations. The absence of mature adaptive immunity enables human xenografting without additional immunosuppression but limits the assessment of tumor interactions with adaptive immune surveillance [6]. Incubation at 34 °C, used as a compromise between zebrafish larval tolerance and human tumor-cell requirements [39], may also alter metabolic and proliferative kinetics relative to physiological human conditions. These features should therefore be considered when extrapolating short-term graft behavior to human tumor biology. Although comparisons between cell lines under the same experimental conditions remain informative, their behavior in the zebrafish microenvironment should not be assumed to fully reproduce the phenotype of the original human tumors.

Finally, daily imaging from 1 to 4 dpi allowed us to characterize only early changes in graft-associated fluorescence.

More broadly, xenograft behavior varied across the four cell lines and two implantation sites, with persistence, organization and dissemination capturing distinct aspects of graft evolution. These observations provide a practical reference for selecting cell lines, implantation sites and observation windows in zebrafish breast cancer studies and for interpreting subsequent assays under comparable experimental conditions.

Supplementary Materials: The following supporting information can be downloaded at https://www.mdpi.com/article/10.3390/life16121981/s1, Figure S1: Representative examples of sphericity measurements in zebrafish xenografts; Figure S2: Cell-free CM-DiI control following perivitelline and yolk-sac microinjection in Casper zebrafish larvae; Figure S3: Assessment of MDA-MB-231 cell viability before and after heat treatment; Figure S4: Morphological comparison of viable and heat-treated MDA-MB-231 cells under zebrafish incubation conditions; Figure S5: Aggregation of heat-treated MDA-MB-231 cells during microinjection; Figure S6: Early characteristics and temporal evolution of perivitelline space (PVS) xenografts following injection of viable and heat-treated MDA-MB-231 cells; Figure S7: Early characteristics and fluorescence organization of yolk-sac xenografts following injection of viable and heat-treated MDA-MB-231 cells; Figure S8: Neutral Red staining of brain microglia after site-specific clodronate-liposome administration in Casper zebrafish larvae; Figure S9: Comparison of circulating-cell detection between Tübingen and Casper zebrafish larvae following MDA-MB-231 PVS implantation. Video S1: Yolk-sac tumor-associated fluorescence redistribution. Data S1: Individual-level numerical data and statistical analyses supporting the main study and additional control experiments.

Author Contributions: Conceptualization, A.-F.B., A.-N.C., P.-A.P. and G.-M.D.; Methodology, A.-F.B. and A.-N.C.; Formal Analysis, A.-F.B. and A.-N.C.; Investigation, A.-F.B. and A.-N.C.; Resources, P.-A.P.; Data Curation, A.-F.B. and A.-N.C.; Writing—Original Draft Preparation, A.-F.B. and A.-N.C.; Writing—Review & Editing, G.-M.D. and P.-A.P.; Supervision, G.-M.D.; Project Administration, G.-M.D.; Funding Acquisition, G.-M.D. All authors have read and agreed to the published version of the manuscript.

Funding: This research and its associated Article Processing Charge were funded by the "Dr. Laser" project ("Aplicații medicale ale laserilor de mare putere"), SMIS 326475, administered through the Regional Institute of Oncology, Iasi, Romania.

Institutional Review Board Statement: The animal study protocol was approved by the ethics committees of Alexandru Ioan Cuza University of Iasi, Romania (Approval No. 693, dated 11 February 2026), Grigore T. Popa University of Medicine and Pharmacy, Iasi, Romania (Approval No. 257, dated 17 January 2023), and the Regional Institute of Oncology, Iasi, Romania (Approval No. 1394, dated 29 November 2022).

Informed Consent Statement: Not applicable.

Data Availability Statement: The data supporting the findings of this study, including the individual-level numerical data underlying the figures and statistical analyses, are available at https://doi.org/10.7910/DVN/FGBD71.

Conflicts of Interest: The funding source had no role in the design of the study, data collection, analysis, interpretation of the results, manuscript preparation, or the decision to publish. The authors declare no conflicts of interest.

Abbreviations

The following abbreviations are used in this manuscript:

CC	Circulating cells
DoC	Duct of Cuvier
dpi	Days post-injection

HER2	Human epidermal growth factor receptor 2
hpf	Hours post-fertilization
PVS	Perivitelline space
TMF	Tail metastatic foci
TNBC	Triple-negative breast cancer

References

1. Sung, H.; Filho, A.M.; Ferlay, J.; Laversanne, M.; Siegel, R.L.; Soerjomataram, I.; Jemal, A.; Bray, F. Global Cancer Statistics 2024: GLOBOCAN Estimates of Incidence and Mortality Worldwide for 34 Cancers in 186 Countries. *CA Cancer J. Clin.* **2026**, *76*, e70090. [CrossRef] [PubMed]
2. Harbeck, N.; Penault-Llorca, F.; Cortes, J.; Gnant, M.; Houssami, N.; Poortmans, P.; Ruddy, K.; Tsang, J.; Cardoso, F. Breast Cancer. *Nat. Rev. Dis. Primers* **2019**, *5*, 66. [CrossRef] [PubMed]
3. Dent, R.; Trudeau, M.; Pritchard, K.I.; Hanna, W.M.; Kahn, H.K.; Sawka, C.A.; Lickley, L.A.; Rawlinson, E.; Sun, P.; Narod, S.A. Triple-Negative Breast Cancer: Clinical Features and Patterns of Recurrence. *Clin. Cancer Res.* **2007**, *13*, 4429–4434. [CrossRef] [PubMed]
4. Ignatov, A.; Eggemann, H.; Burger, E.; Ignatov, T. Patterns of breast cancer relapse in accordance to biological subtype. *J. Cancer Res. Clin. Oncol.* **2018**, *144*, 1347–1355. [CrossRef] [PubMed]
5. Fior, R.; Póvoa, V.; Mendes, R.V.; Carvalho, T.; Gomes, A.; Figueiredo, N.; Ferreira, M.G. Single-cell functional and chemosensitive profiling of combinatorial colorectal therapy in zebrafish xenografts. *Proc. Natl. Acad. Sci. USA* **2017**, *114*, E8234–E8243. [CrossRef] [PubMed]
6. Lam, S.H.; Chua, H.L.; Gong, Z.; Lam, T.J.; Sin, Y.M. Development and Maturation of the Immune System in Zebrafish, Danio Rerio: A Gene Expression Profiling, in Situ Hybridization and Immunological Study. *Dev. Comp. Immunol.* **2004**, *28*, 9–28. [CrossRef] [PubMed]
7. Rosowski, E.E. Determining Macrophage versus Neutrophil Contributions to Innate Immunity Using Larval Zebrafish. *Dis. Model. Mech.* **2020**, *13*, dmm041889. [CrossRef] [PubMed]
8. Póvoa, V.; Rebelo de Almeida, C.; Maia-Gil, M.; Sobral, D.; Domingues, M.; Martinez-Lopez, M.; de Almeida Fuzeta, M.; Silva, C.; Grosso, A.R.; Fior, R. Innate Immune Evasion Revealed in a Colorectal Zebrafish Xenograft Model. *Nat. Commun.* **2021**, *12*, 1156. [CrossRef] [PubMed]
9. Sturtzel, C.; Grissenberger, S.; Bozatzi, P.; Scheuringer, E.; Wenninger-Weinzierl, A.; Zajec, Z.; Dernovšek, J.; Pascoal, S.; Gehl, V.; Kutsch, A.; et al. Refined High-Content Imaging-Based Phenotypic Drug Screening in Zebrafish Xenografts. *npj Precis. Oncol.* **2023**, *7*, 44. [CrossRef] [PubMed]
10. Cornet, C.; Dyballa, S.; Terriente, J.; Di Giacomo, V. ZeOncoTest: Refining and Automating the Zebrafish Xenograft Model for Drug Discovery in Cancer. *Pharmaceuticals* **2020**, *13*, 1. [CrossRef] [PubMed]
11. Subik, K.; Lee, J.F.; Baxter, L.; Strzepek, T.; Costello, D.; Crowley, P.; Xing, L.; Hung, M.C.; Bonfiglio, T.; Hicks, D.G.; et al. The Expression Patterns of ER, PR, HER2, CK5/6, EGFR, Ki-67 and AR by Immunohistochemical Analysis in Breast Cancer Cell Lines. *Breast Cancer* **2010**, *4*, 35–41. [CrossRef]
12. Gazdar, A.F.; Kurvari, V.; Virmani, A.; Gollahon, L.; Sakaguchi, M.; Westerfield, M.; Kodagoda, D.; Stasny, V.; Cunningham, H.T.; Wistuba, I.I.; et al. Characterization of Paired Tumor and Non-Tumor Cell Lines Established from Patients with Breast Cancer. *Int. J. Cancer* **1998**, *78*, 766–774. [CrossRef]
13. Cani, O.; Zannotti, L.; De Vita, A.; Liverani, C.; Vanni, S.; Miserocchi, G. Zebrafish Tumor Xenograft Models for Drug-Screening: A Systematic Review of Methods for Treatment Assessment. *J. Transl. Med.* **2026**, *24*, 417. [CrossRef] [PubMed]
14. Drabsch, Y.; He, S.; Zhang, L.; Snaar-Jagalska, B.E.; ten Dijke, P. Transforming Growth Factor-β Signalling Controls Human Breast Cancer Metastasis in a Zebrafish Xenograft Model. *Breast Cancer Res.* **2013**, *15*, R106. [CrossRef] [PubMed]
15. Larsson, P.; Pettersson, D.; Olsson, M.; Sarathchandra, S.; Abramsson, A.; Zetterberg, H.; Ittner, E.; Forssell-Aronsson, E.; Kovács, A.; Karlsson, P.; et al. Repurposing Proteasome Inhibitors for Improved Treatment of Triple-Negative Breast Cancer. *Cell Death Discov.* **2024**, *10*, 57. [CrossRef] [PubMed]
16. Rong, X.; Chen, H.; Guo, X.; Sun, X.; Li, L.; Ye, Y.; Li, C.; Nian, S.; Liang, C.; Yuan, Q. Zebrafish Xenografts in Breast Cancer Research. *Front. Immunol.* **2025**, *16*, 1540610. [CrossRef] [PubMed]
17. Gámez-Chiachio, M.; Molina-Crespo, Á.; Ramos-Nebot, C.; Martinez-Val, J.; Martinez, L.; Gassner, K.; Llobet, F.J.; Soriano, M.; Hernandez, A.; Cordani, M.; et al. Gasdermin B Over-Expression Modulates HER2-Targeted Therapy Resistance by Inducing Protective Autophagy through Rab7 Activation. *J. Exp. Clin. Cancer Res.* **2022**, *41*, 285. [CrossRef] [PubMed]
18. Lotter, C.; Stierli, M.A.; Puligilla, R.D.; Huwyler, J. Dual Targeted Lipid Nanoparticles for Enhanced DNA Delivery and Transfection of Breast Cancer Cells. *Eur. J. Pharm. Biopharm.* **2025**, *209*, 114674. [CrossRef] [PubMed]

19. Kimmel, C.B.; Ballard, W.W.; Kimmel, S.R.; Ullmann, B.; Schilling, T.F. Stages of Embryonic Development of the Zebrafish. *Dev. Dyn.* **1995**, *203*, 253–310. [CrossRef] [PubMed]
20. Martinez-Lopez, M.; Póvoa, V.; Fior, R. Generation of Zebrafish Larval Xenografts and Tumor Behavior Analysis. *J. Vis. Exp.* **2021**, *172*, e62373. [CrossRef] [PubMed]
21. Haldi, M.; Ton, C.; Seng, W.L.; McGrath, P. Human Melanoma Cells Transplanted into Zebrafish Proliferate, Migrate, Produce Melanin, Form Masses and Stimulate Angiogenesis in Zebrafish. *Angiogenesis* **2006**, *9*, 139–151. [CrossRef] [PubMed]
22. Yang, L.; Rojas, A.M.; Shiau, C.E. Liposomal Clodronate-mediated Macrophage Depletion in the Zebrafish Model. *Bio-Protocol* **2021**, *11*, e3951. [CrossRef] [PubMed]
23. Schindelin, J.; Arganda-Carreras, I.; Frise, E.; Kaynig, V.; Longair, M.; Pietzsch, T.; Preibisch, S.; Rueden, C.; Saalfeld, S.; Schmid, B.; et al. Fiji: An Open-Source Platform for Biological-Image Analysis. *Nat. Methods* **2012**, *9*, 676–682. [CrossRef] [PubMed]
24. Fieuws, C.; Bek, J.W.; Parton, B.; De Neef, E.; De Wever, O.; Hoorne, M.; Estrada, M.F.; Van Dorpe, J.; Denys, H.; Van de Vijver, K.; et al. Zebrafish Avatars: Toward Functional Precision Medicine in Low-Grade Serous Ovarian Cancer. *Cancers* **2024**, *16*, 1812. [CrossRef] [PubMed]
25. Bedell, V.M.; Dubey, P.; Lee, H.B.; Bailey, D.S.; Anderson, J.L.; Jamieson-Lucy, A.; Xiao, R.; Leonard, E.V.; Falk, M.J.; Pack, M.A.; et al. Zebrafishology, Study Design Guidelines for Rigorous and Reproducible Data Using Zebrafish. *Commun. Biol.* **2025**, *8*, 739. [CrossRef] [PubMed]
26. von Herbing, I.H.; Pan, F.T.C. Multiple Stressors, Allostasis and Metabolic Scaling in Developing Zebrafish. *J. Exp. Biol.* **2022**, *225*, jeb244095. [CrossRef] [PubMed]
27. Teng, Y.; Xie, X.; Walker, S.; White, D.T.; Mumm, J.S.; Cowell, J.K. Evaluating Human Cancer Cell Metastasis in Zebrafish. *BMC Cancer* **2013**, *13*, 453. [CrossRef] [PubMed]
28. Xiao, J.; McGill, J.R.; Nasir, A.; Lekan, A.; Johnson, B.; Wilkins, D.J.; Pearson, G.W.; Tanner, K.; Goodarzi, H.; Glasgow, E.; et al. Identifying Drivers of Breast Cancer Metastasis in Progressively Invasive Subpopulations of Zebrafish-Xenografted MDA-MB-231. *Mol. Biomed.* **2022**, *3*, 16. [CrossRef] [PubMed]
29. Marques, I.J.; Weiss, F.U.; Vlecken, D.H.; Nitsche, C.; Bakkers, J.; Lagendijk, A.K.; Partecke, L.I.; Heidecke, C.D.; Lerch, M.M.; Bagowski, C.P. Metastatic Behaviour of Primary Human Tumours in a Zebrafish Xenotransplantation Model. *BMC Cancer* **2009**, *9*, 128. [CrossRef] [PubMed]
30. Follain, G.; Osmani, N.; Azevedo, A.S.; Allio, G.; Mercier, L.; Karreman, M.A.; Solecki, G.; Garcia Leòn, M.J.; Lefebvre, O.; Fekonja, N.; et al. Hemodynamic Forces Tune the Arrest, Adhesion, and Extravasation of Circulating Tumor Cells. *Dev. Cell* **2018**, *45*, 33–52.e12. [CrossRef] [PubMed]
31. Franchi-Mendes, T.; Lopes, N.; Brito, C. Heterotypic Tumor Spheroids in Agitation-Based Cultures: A Scaffold-Free Cell Model That Sustains Long-Term Survival of Endothelial Cells. *Front. Bioeng. Biotechnol.* **2021**, *9*, 649949. [CrossRef] [PubMed]
32. Arnaldi, P.; Zotti Delli, V.; Bellese, G.; Gagliani, M.C.; Orecchia, P.; Castagnola, P.; Cortese, K. 3D Breast Cancer Spheroids Reveal Architecture-Dependent HER2 Expression and Signaling. *Biology* **2025**, *14*, 1654. [CrossRef] [PubMed]
33. Pierceall, W.E.; Woodard, A.S.; Morrow, J.S.; Rimm, D.; Fearon, E.R. Frequent Alterations in E-Cadherin and Alpha- and Beta-Catenin Expression in Human Breast Cancer Cell Lines. *Oncogene* **1995**, *11*, 1319–1326. [PubMed]
34. de Abreu Pereira, D.; Sandim, V.; Fernandes, T.F.B.; Almeida, V.H.; Rocha, M.R.; do Amaral, R.J.F.C.; Rossi, M.I.D.; Kalume, D.E.; Zingali, R.B. Proteomic Analysis of HCC-1954 and MCF-7 Cell Lines Highlights Crosstalk between αv and β1 Integrins, E-Cadherin and HER-2. *Int. J. Mol. Sci.* **2022**, *23*, 10194. [CrossRef] [PubMed]
35. Ivascu, A.; Kubbies, M. Diversity of Cell-Mediated Adhesions in Breast Cancer Spheroids. *Int. J. Oncol.* **2007**, *31*, 1403–1413. [CrossRef]
36. Dang, T.T.; Prechtl, A.M.; Pearson, G.W. Breast Cancer Subtype-Specific Interactions with the Microenvironment Dictate Mechanisms of Invasion. *Cancer Res.* **2011**, *71*, 6857–6866. [CrossRef] [PubMed]
37. Sebastian, A.; Hum, N.R.; Martin, K.A.; Gilmore, S.F.; Peran, I.; Byers, S.W.; Wheeler, E.K.; Coleman, M.A.; Loots, G.G. Single-Cell Transcriptomic Analysis of Tumor-Derived Fibroblasts and Normal Tissue-Resident Fibroblasts Reveals Fibroblast Heterogeneity in Breast Cancer. *Cancers* **2020**, *12*, 1307. [CrossRef] [PubMed]
38. Dryer, Y.; Berghausen, J.; Creswell, K.; Glasgow, E.; Brelidze, T.I. Comparison of Tumor Growth Assessment Using GFP Fluorescence and DiI Labeling in a Zebrafish Xenograft Model. *Cancer Biol. Ther.* **2023**, *24*, 2234140. [CrossRef] [PubMed]
39. Cabezas-Sainz, P.; Coppel, C.; Pensado-López, A.; Fernandez, P.; Muinelo-Romay, L.; López-López, R.; Rubiolo, J.A.; Sánchez, L. Morphological Abnormalities and Gene Expression Changes Caused by High Incubation Temperatures in Zebrafish Xenografts with Human Cancer Cells. *Genes* **2021**, *12*, 113. [CrossRef] [PubMed]

Disclaimer/Publisher's Note: The statements, opinions and data contained in all publications are solely those of the individual author(s) and contributor(s) and not of MDPI and/or the editor(s). MDPI and/or the editor(s) disclaim responsibility for any injury to people or property resulting from any ideas, methods, instructions or products referred to in the content.